Article

Fabrication, Characterization, and Biological Evaluation of *T. terrestris* Incorporated Titanium-Doped ZnO/Cellulose Nanocomposite Films as a Therapeutic Hemostatic Scaffolds for Diabetic Wound Healing

Jijo Thomas Koshy, Dhanaraj Sangeetha,* Yogesh Bele, and Murugan Rakshitha

Read Online

| ACCESS | Metrics & More | Article Recommendations | SI Supporting Information |

ABSTRACT: The advent of biobased materials exhibiting remarkable effectiveness and performance has ushered in a paradigm shift in the field of biomedical science. Polymers are often used in the medical sector, particularly in the regeneration of bones, tissues, and wounds. Fast wound healing and self-healing polymers created from sustainable surroundings are attractive alternatives to create demand for new pathways in polymer research. This study investigates the efficacy of a biowaste-derived polymer, which was extracted and supplemented with titanium-doped ZnO nanoparticles along with medication in the form of an extract to evaluate its effectiveness in promoting wound healing. The prepared materials were further characterized using X-ray diffraction (XRD), UV−visible spectroscopy, Fourier-transform infrared spectroscopy (FTIR), field emission scanning electron microscopy (FE-SEM), optical microscopy, atomic force microscopy (AFM), tensile, and its color parameters. In vitro studies on wound healing were also conducted. The results clearly showed that the produced substance possesses properties that are noteworthy for wound healing.
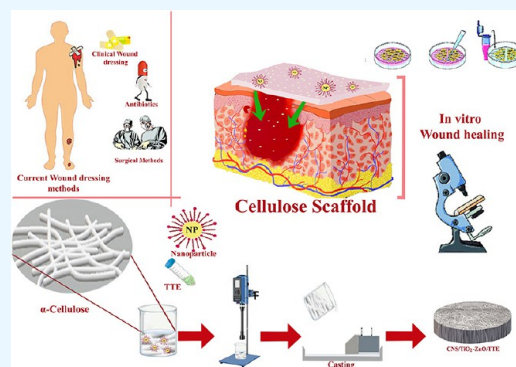
1. INTRODUCTION

Wound healing is a complex phenomenon characterized by the passage of numerous intricate phases in which interactions between cells and between cells and the matrix are critical. In order to facilitate a more rapid healing process, it is necessary to use a variety of dressing materials due to the intricacy of wounds. An extensive range of dressing materials are currently available in the market; however, among these, those that incorporate Ayurvedic medicines for optimal efficacy stand out as a crucial factor.[1] Breaching the skin can cause physiological imbalances in the body, which can be lethal. It is estimated that more than 6.5 million people have chronic skin wounds, including diabetic foot ulcers, venous ulcers, pressure sores, and injuries from accidents.[2] Bioactive wound dressings, which not only promote extracellular matrix (ECM) deposition regulation but also expedite the healing process, are essential for preventing additional complications associated with fibrosis. Thus, in order to achieve aesthetic wound repair, it is critical to utilize effective wound dressings that target all four phases of the wound healing process.[3] The dynamic process of wound healing requires the interaction of several cell types, along with an ideal extracellular environment. These interactions between blood components, extracellular matrix, and cellular growth factors facilitate the healing of wounds. Cytokines facilitate the process of healing through diverse mechanisms, such as stimulating the development of granulation tissue, preventing dehydration, and promoting the formation of basement membrane components.[4]

Wounds that occur in everyday life, vehicle accidents, and fires require immediate medical attention because the damaged skin loses its capacity to act as an infection barrier.[5] Artificial skin patches and a range of synthetic drugs are frequently utilized for wound healing.[6,7] Natural polymer-based macromolecular nanocarriers are ideal for therapeutic applications due to their complex branching structure, which allows for functionalization via diverse chemical interactions.[8] For instance, the nontoxicity, biocompatibility, and biodegradability of natural hydrophilic polysaccharide-based drug delivery systems render them more advantageous in the fields of tissue engineering, antimicrobial, and anticancer therapeutics.[9] Cellulose, which is the most prevalent polysaccharide on earth, is primarily responsible for the mechanical stability of plants and is also utilized by humans in a wide variety of
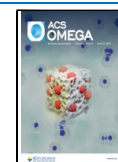
uses.[10,11] Biomedical applications of cellulose are becoming more feasible as soluble cellulose derivatives with diverse functional moieties along the backbone and modified nanocellulose with versatile surface functional groups are developed. These advancements are made possible by the native features of cellulose, which include both cellulose chains and supramolecular-ordered domains in the form of extractable nanocellulose. About half of the carbon in lignocellulosic biomass is found in cellulose, which is a β(1−4)-linked chain of glucose molecules.[12,13] Therefore, this macromolecule has attracted a lot of attention as a sustainable and renewable supply and prompted scientists to create cellulose-based products with innovative uses.[14]

Nowadays, cellulose nanocrystals have been incorporated into sustained-release capsules, microparticles, aerogels, and hydrogels for drug delivery.[15] Because of their widespread applications, nanoparticles are the most researched area of interest. Nevertheless, the nanoparticles may cluster and become challenging to disperse in water based on their chemical makeup. This can be avoided by coating the nanoparticles with the appropriate surfactants. The surfactant's hydrophobic groups provide stability and steric hindrance when the nanoparticles are in close proximity to one another. Surfactants are surface active chemicals, similar to detergents, that promote spreading and wetting capabilities by lowering the surface tension of a liquid. Surfactant-coated nanoparticles offer an alternative perspective for applications in food technology and nanomedicine. Surfactants are amphiphilic substances, meaning that their chemical structures contain both hydrophilic and hydrophobic functionalities. Additionally, surfactant-coated nanoparticles have a significant impact on building materials, coatings, and paints.[16,17]

Plants and herbs have been used for the treatment of chronic diseases because of their crucial pharmacological properties, including their ability to minimize drug resistance, alleviate systemic toxicities, reduce the need for synthetic chemotherapeutic drugs, and enhance the immune system.[18] The genus Tribulus, which belongs to the Zygophyllaceae family, has roughly 20 different species, three of which are common in India: Tribuluscistoides, Tribulusalatus, and *T. terrestris*. In liver cancer cells, the *T. terrestris* extract (TTE) has been demonstrated to suppress cell proliferation and increase apoptosis. Its biological activity is similar to that of steroidal saponins in that it induces an apoptotic pathway in breast cancer cells. Alkaloids, resins, flavonoid oil, and nitrates are found in TTE and possess antihypertensive, anti-inflammatory, hypolipidemic, and antidiabetic properties.[19] According to reports, *T. terrestris*' ethanolic extract dramatically reduced abnormal levels of serum glucose, triglycerides, and cholesterol in Streptozotocin (STZ)-induced diabetic rats and it also demonstrated strong antioxidant action against these mice.[20,21] In this study, we employ a casting technique to fabricate a polymeric scaffold containing an ayurvedic medication and nanocomposites. The source of cellulose was derived from sugar cane bagasse, extracted via steam explosion. Furthermore, we chose TiO$_2$-doped ZnO nanoparticles as the filler, and *T. terrestris* was used as an ayurvedic drug to enhance the wound-healing property of cellulose film. Supportive in vitro research was conducted to determine the efficacy of polymer scaffolds in wound healing.

2. MATERIALS AND METHODS

2.1. Materials Used. Zinc acetate [Zn(CH$_3$COO)$_2$·2H$_2$O, M_w = 219.50], sodium hydroxide, titanium iso-propoxide, concentrated hydrochloric acid, citric acid, cetyltrimethylammonium bromide, sodium hypochlorite, ethanol were purchased from Nice Chemicals, Bengaluru. Polyvinyl alcohol (PVA; M. wt. 115,000), DMEM medium, fetal bovine serum, 1% antibiotic cocktail, cell-grade DMSO. All the chemicals used were of analytical grade.

2.2. Extraction of Cellulose. Sugar cane bagasse is the main residue of the sugar cane industry and a promising renewable and sustainable lignocellulosic material.[22] High-purity cellulose fibers were extracted by steam explosion process followed by bleaching.[23] The conversion of lignocellulosic biomass to high-purity nanocellulose is through three steps: acid treatment, alkaline treatment, and bleaching. The methodology of the earlier research was changed in accordance with the specifications. X-ray diffraction was used to characterize the isolated cellulose fibers. The extraction procedure is attached as Supporting Information (Figure S1). After all of the treatment, the hydrolyzed cellulose samples were washed several times and submitted to a centrifugation stage (7000 rpm) for 20 min. Then, the cellulose was sonicated with an ultraprobe sonicator for proper dispersion (Figure 1). After
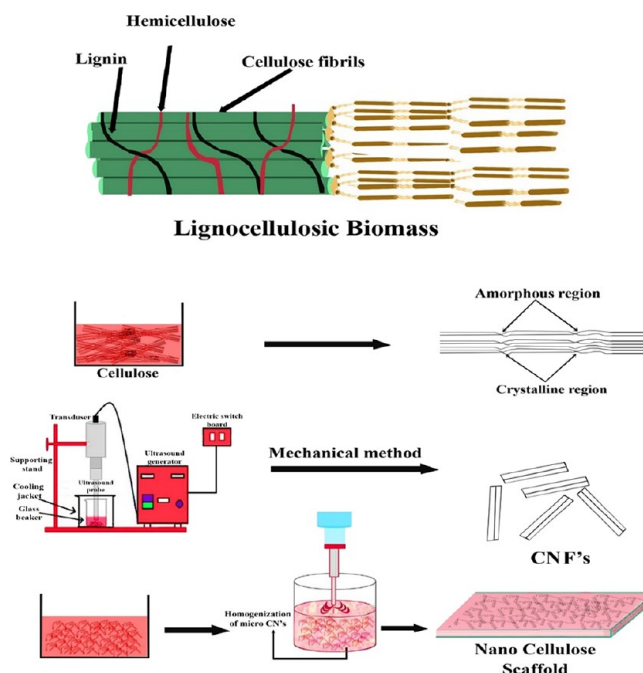

Figure 1. Cellulose scaffold preparation from lignocellulosic biomass.

each washing step, the crystals were separated from the solution and oven-dried at 80 °C. The yield was calculated using the equation

$$\text{Yield (\%)} = \frac{W_{\text{initial}} - W_{\text{final}}}{W_{\text{initial}}} \times 100 \tag{1}$$

where W_{initial} is the initial weight and W_{final} is the final weight.

2.3. Synthesis of Nanocomposite and Extraction of TTE. Titanium-doped zinc oxide nanocomposite was synthesized by the sol−gel method. For the synthesis, zinc acetate and titanium iso-propoxide were used as precursors.[24] The nanocomposites were prepared by coating them with CTAB

surfactant. The structural and morphological analyses were carried out by X-ray diffraction and FE-SEM respectively. For the extraction of TTE, a total of 10 g of *T. terrestris* seed powder was weighed, and a required volume of ethanol was added for Soxhlet extraction with six cycles. The extract was centrifuged and filtered by using Whatman filter paper. The filtered extract was stored in a glass container and placed in a dark environment.

2.4. Preparation of Cellulose Film. The casting method was used to prepare the film samples: C (cellulose), CNP (C−Ti/ZnO), and CNPE (C−Ti/ZnO-TTE). A total volume of 100 mL of cellulose containing 5% PVA (hot water-soluble) was mechanically mixed and cast at 50 °C for 12 h. The other two films were made in the same way, with 0.025 g of produced nanocomposite and 10 mL of seed extract. X-ray diffraction and Fourier transform infrared spectroscopy were used to investigate the produced film samples. The morphology and texture of the film samples were examined using FE-SEM and AFM.

2.5. Characterization of Extract. The antimicrobial activity of the extract was carried out through the conventional Kirby−Bauer test or disc diffusion method.[25] Antibacterial activity was performed utilizing a modified agar well diffusion method. The sterile Muller Hinton Agar plates were splattered with approximately 0.2 mL of the standard 24 h-old broth culture of the test organisms. Afterward, they were permitted to harden. Wells of an approximate diameter of 6 mm were drilled into the plates by utilizing a sterile cork borer. After dispensing the prepared ethanol extract into the wells, they were left undisturbed for approximately 15 min to facilitate prediffusion of the extract. The dishes were subsequently incubated for 24 h at 37 °C. Inhibition zones that had formed on the agar plates during the incubation period for each of the utilized bacterial strains were observed, quantified, and tabulated. The standard gentamycin was kept as a positive control.

A color sensor was utilized for measuring the color parameters of *T. terrestris* and TTE. The lightness (L^*), greenness (a^*) and yellowness (b^*) were measured. ΔE is calculated to identify the difference between two colors in an $L^*a^*b^*$ color space. The gravimetric method, which is an extensively used laboratory technique in numerous industries (e.g., food, construction, textiles, agriculture, and chemicals), was employed for moisture analysis in accordance with WHO guidelines.[26] The sample is weighed about 1.5 g in a porcelain dish, dried in the oven at 100 or 105 °C, cooled in a desiccator, and weighed. The loss of weight is usually recorded as moisture. The moisture content is calculated based on the initial and final weights of the sample, which assumes that all weight loss is due to the removal of water and ignores the loss of other volatiles. The percentage moisture of the extract is calculated by using the eq 2.

$$\%\text{Moisture} = \frac{\text{Wt of wet sample} - \text{Wt of dry sample}}{\text{Wt of wet sample}} \times 100 \quad (2)$$

About 0.5 g of plant powder should be added to dry, clean test tubes for UV fluorescence analysis. Five ml of various organic solvents, such as distilled water, ethanol, methanol, ethyl acetate, acetone, chloroform, petroleum ether, acetic acid, 4 N HNO₃, 4 N H₂SO₄, 4 N HCl, and 10% NaOH, were added individually to each glass bottle. After shaking each tube, they

were left to stand for 20−25 min. For their distinctive color, the solutions were examined in visible daylight, short-wavelength UV light (254 nm), and long-wavelength UV light (365 nm).

The ash value is used to determine the quality and purity of a crude drug and to establish its identity. Ash contains inorganic radicals like phosphates, carbonates, and silicates of sodium, potassium, magnesium, calcium, etc. These are present in definite amounts in a particular crude drug; hence, quantitative determination in terms of various ash values helps in their standardization. Two grams of powder were weighed into a silica crucible and ignited at 450 °C. The total ash value is calculated by the following eq 3

$$\text{Total ash value of the sample} = \frac{100(z - x)}{y}\% \quad (3)$$

where x is the weight of the empty dish, y is the weight of the sample taken, and z is the weight of the dish and total ash.

2.6. Characterization of Cellulose. XRD pattern of extracted cellulose and nanocellulose scaffold were analyzed using an X-ray powder diffractometer (Bruker D8 Advance, Germany) with Cu k radiation ($\lambda = 1.5405$ Å) in a 2θ (deg) (Bragg angle) range ($10°−90°$) at a scanning rate of $4°$/min was utilized. Fourier Transform Infrared Spectroscopy (ALPHA T, Bruker) was used to analyze functional groups with a range of $4000−400$ cm^{-1} in ATR mode. The film morphology was examined using field emission scanning electron microscopy, and atomic force microscopy. FE-SEM, with a Carl-Zeiss Model Ultramicroscope-55 (German). AFM (Nanosurf easy scan2 Nanosurf AG Switzerland 23-06-154) was used to more precisely characterize the surface morphology of the materials. AFM is a methodology that can generate a topographic map of the sample surface by leveraging the interactions that occur between the tip and the sample surface. The surface morphology of the sample can be observed by the use of laser data collection on the cantilever's deflection. The texture of the film (1 by 1 cm) was captured using an optical microscope (upright optical microscope Olympus BX61) and optical stream motion software at two different magnifications, 20 and 50 μm.

The color and transparency of the composite films with different compositions on a white background plate were assessed using a colorimeter (Nix mini 2 color sensor). Three points were chosen at random to repeat the experiment after each film was cut into squares (2×2 cm). L^* (lightness/brightness), a^* (redness/greenness), and b^* (yellowness/blueness) are used to describe the parameters.[27] The following formula (eq 4) is used to determine the color parameters of the film:

$$\Delta E^* = \sqrt{(\Delta L^*)^2 + (\Delta a)^{*2}(\Delta b)^{*2}} \quad (4)$$

where ΔL^*, Δa^*, and Δb^* are the differences in the sample and control values for the respective color parameters ($L^* = 72.3$, $a^* = 0.3$, $b^* = 16.7$).

Whiteness index (WI) (eq 5) and Yellowness Index (YI) (eq 6) were measured. Each sample measurement was performed in triplicate. The results were then performed as standard means of measurements.

Whiteness Index (WI)

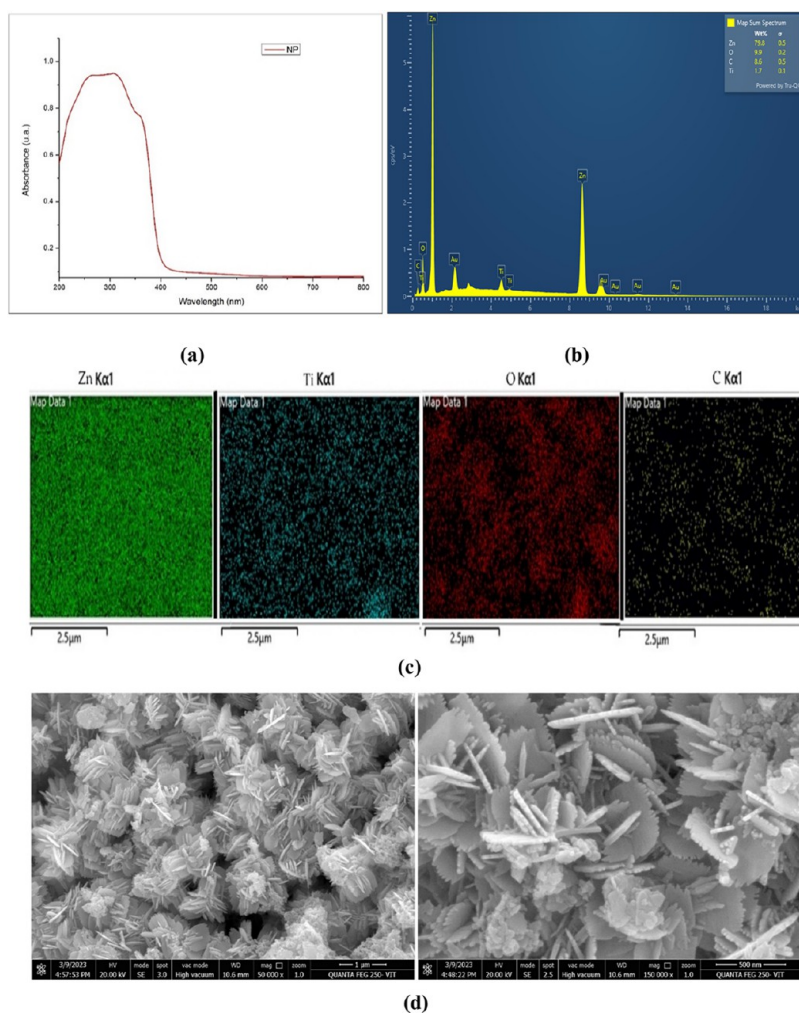$$= 100 - \sqrt{((100 - L_0)^2 + a_0{}^2 + b_0{}^2)} \quad (5)$$

Figure 2. (a) UV−visible spectrum of nanoparticle. (b) EDX of Ti/ZnO. (c) FESEM Elemental mapping of nanocomposites. (d) FE-SEM image of Ti/ZnO nanocomposite.

$$\text{Yellowness Index (YI)} = 142.86 \frac{b_0}{L_0} \qquad (6)$$

Mechanical parameters such as the tensile strength (TS) and elongation at break percentage (E) were investigated. The tensile properties of the material (12.5 × 1.5 cm) were determined by using a Tinius Olsen instrument during the tensile analysis. The tensile analysis was carried out in accordance with the ASTM standard (ASTM D882-18). The cross-head speed was adjusted to 50 mm/min. The ultimate tensile strength and elongation at break were determined by using Horizon software.

The liquid displacement method was used for performing porosity studies of the prepared films. The preweighed film (2 cm × 2 cm) was placed in a beaker containing 5 mL of absolute ethanol for 24 h. After removal from the ethanol, the films were weighed and examined to determine porosity. The porosity of films was calculated using the formula below (eq 7).[28]

$$\text{Porosity, } P = \frac{(W_Y - W_X - W_Z)}{(W_Y - W_Z)} \times 100 \qquad (7)$$

W_x is the initial weight of films, W_y is the combined weight of the immersed film and ethanol, and W_z is the weight of ethanol after removing the film.

For the dressing pH analysis, all the prepared nanocomposite films were first divided into 2 cm × 2 cm samples and subjected to dip in a saline solution for 24 h. Using a digital pH meter and the same solution, the dressing pH was measured following the designated observation period after each film was removed from the standard saline solution. The results were obtained by triplicating the sample and recording the average values.

Glucose uptake assay is carried out by Suthar et al. with slight modifications and performed with L6 cells.[29] Cells were grown in 48-well plates and incubated in a CO_2 incubator for 48 h at 37 °C. The culture has been mixed with serum-free DMEM containing 0.2% BSA once a semiconfluent monolayer had developed, and it was then incubated for 18 hours at 37 °C in a CO_2 incubator. After 18 h, the medium was removed, and the cells were washed once with PBS (pH 7.4) buffer and treated for 1 h with 1000 g/mL glucose and test compound (25, 50, 100 g/mL). The difference between the initial and final glucose concentrations in the incubated medium was utilized to determine glucose uptake. The final glucose concentration was calculated by using the anthrone technique and a glucose standard graph.

For the scratch wound healing assay, cells (1 million cells/well) were grown on 6-well plates and allowed to acclimatize to the culture conditions of 37 °C and 5% CO_2 in the incubator
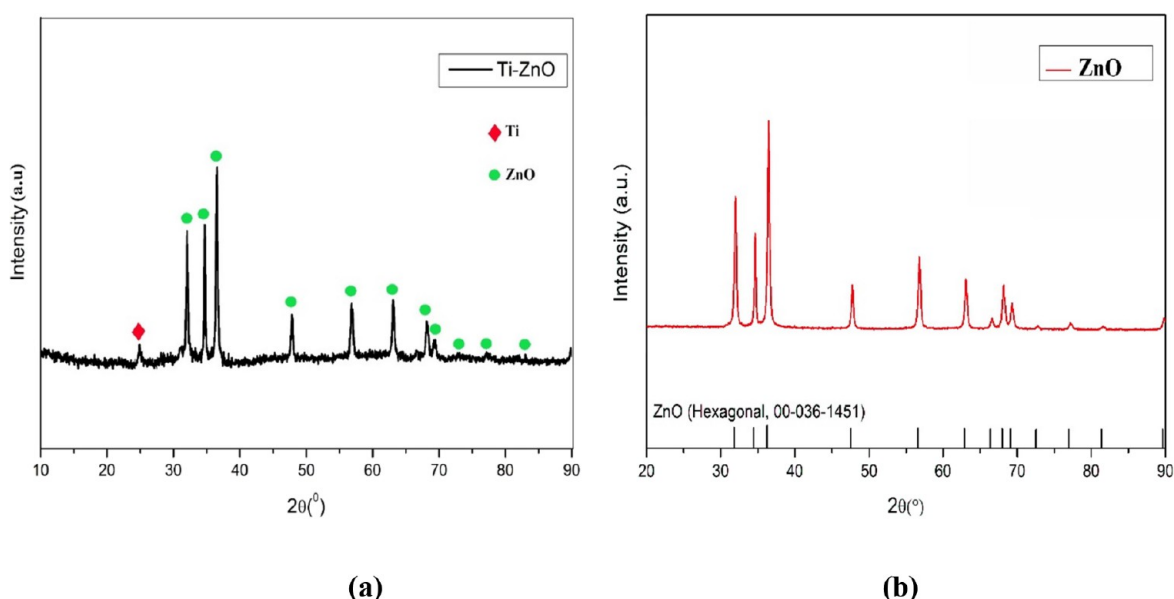
Figure 3. XRD spectra of (a) Ti-ZnO and (b) Pure ZnO.

for 24 h. The test samples were sterilized using a 0.2 μm Millipore syringe filter after being prepared in cell culture grade DMSO (10 mg/mL). After diluting the samples in DMEM media, final concentrations of 25, 50, and 100 μg/mL were added to wells containing cultured cells that had reached a confluency of at least 80%. Untreated wells are used as a control. Before starting tests on scratch wound healing, it is necessary to scrape the cell monolayer in a straight line to generate a "scratch." This can be accomplished by using a 200 μL pipet tip. The debris was removed and the edge of the scratch was smoothed by rinsing the cells once with 1 mL of growth medium and then replacing it with 5 mL of new medium. The area near the scratch was marked with markers to serve as reference points in order to capture the same field during the image-gathering process. The well plate can be delicately etched on the outside of the dish with a razor blade or an ultrafine tip marker to provide the reference points. The dish was placed under a phase-contrast microscope after making the reference points, making sure the reference mark was outside the capture picture field but inside the eyepiece field of view. Then, the initial picture of the scratch was obtained. A tissue culture incubator set to 37 °C should be utilized for preserving the well plate. Different time intervals (0, 12, 24, and 36 h) were utilized to capture photomicrographs. Depending on the specific cell type being employed, the incubation period should be empirically determined.[27] Periodically, the well plates can be removed from the incubator for examination, and then, they can be put back in to continue incubating.

2.7. Statistical Analysis. The measurements for each film were conducted three times, and the results were provided as the mean values with the standard deviation. A statistically significant difference ($p < 0.05$) was determined with the help of IBM SPSS software, employing a one-way analysis of variance (ANOVA) and Duncan's multiple range test.

3. RESULTS AND DISCUSSION

3.1. Characterization of Nanoparticle and Extract.
3.1.1. UV−Visible Spectrum of Nanoparticles. The optical properties were studied by using UV−visible spectroscopy.

Table 1. Crystallite Size of Prepared Nanocomposites

		Miller indices				
2θ	d (Å)	h	k	l	fwhm (β)	crystallite size D(nm)
25.47°	3.495	1	0	1	0.578	14.717
31.85°	2.789	1	0	0	0.193	44.707
34.47°	2.583	0	0	2	0.241	36.084
36.43°	2.457	1	0	1	0.241	36.245
47.6°	1.901	1	0	2	0.385	23.554
56.69°	1.617	1	1	0	0.385	24.487
63.13°	1.472	1	0	3	0.289	33.695
68.14°	1.374	1	1	2	0.579	17.299
69.15°	1.351	2	0	1	0.579	17.404

Table 2. Elemental Composition of Nanocomposite

element	wt %	Σ
Zn	79.8	0.5
O	9.9	0.2
Ti	1.7	0.1

Table 3. Zone of Inhibition Value of TTE

	zone of inhibition	
organism	control	TTE
Gram-positive		
S. aureus	23 mm	16 mm
Gram-negative		
E. coli	24 mm	18 mm

Figure 2a shows the UV−visible absorption spectra of the titanium-doped ZnO powders. It is a widely used technique to study the electronic transitions and energy band structure of metallic nanoparticles. In the UV−visible spectrum of Ti/ZnO nanoparticles, the absorbance spectrum is obtained over a wide range of wavelengths from ultraviolet to visible region. The absorbance of light by nanoparticles is due to the transition of electrons between different energy levels. The titanium-doped ZnO powders, which were made from zinc acetate, have absorption margins that are close to 400 nm, as shown in
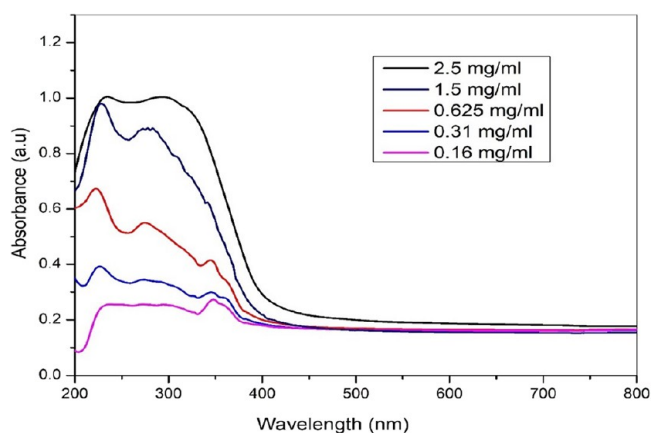
Figure 4. UV absorbance spectra of TTE with different concentrations.

Figure 2a. The particles' absorption edge wavelength is less than 400 nm, as shown in Figure 2a. This can be demonstrated that the absorption edge shift of the powders is caused by the particle size and crystal structure because the zincite ZnO's absorption edge is 387 nm.[30] The titanium-doped ZnO powders exhibit an improved quantum size effect and a reduction in the particle size upon synthesis from zinc acetate. Similarly, when titanium penetrates the zinc oxide crystal lattice, the crystal lattice ruptures and reduces the band gap. This results in the existence of the redshift effect. The results of UV−visible spectroscopy can provide valuable information for the optimization of the properties of Ti/ZnO nanocomposites for various applications.

3.1.2. XRD of Zn−Ti Nanocomposites. Figure 3a,b shows the phase composition of prepared Ti-doped ZnO and pure ZnO nanoparticles calcined at 500 °C. The figure, which includes prepared nano forms with CTAB as surfactant. From the above figure depicts the composites are all crystalline and having diffraction peaks at 2θ value ranging 31.85°, 34.47°, 36.43°, 47.6°, 56.69°, 63.13°, 68.14°, 69.15°, 72.67°, 77.09°, 81.43°, and 89.70° labeled by their Miller indices (1 0 0), (0 0

2), (1 0 1), (1 0 2), (1 1 0), (1 0 3), (2 0 0), and (1 1 2) corresponds to the ZnO (JCPDS no. 00-036-1451) (Figure 3b) with hexagonal wurtzite phase. From Figure 3a it is evident that the presence of Ti-doped in Zn corresponds to the 2θ value of 25.47° and the Anatase phase (Anatase, JCPDS No. 21-1272) of TiO_2 (1 0 1). There is a shift in position because of the influence of CTAB as a surfactant. The formation of anatase was observed at 500 °C. The crystallite size of the anatase phase was increased to 14.71 nm compared with previous studies.[31] The particle dispersed all over the ZnO surface, so the intensity of the peak is very low. The concentration of TiO_2 is very small so there is a very less intense peak found. Compared with pure ZnO and TiO_2-doped ZnO, the intensity of the peak increased. The crystallite size (D) of prepared ZnO doped by TiO_2 nanocomposites can be calculated by Scherrer's formula in (eq 8):[32,33]

$$D = \frac{0.94\lambda}{\beta \cos \theta} \tag{8}$$

where D denotes the average crystallite size of the particle, 0.94 is the Scherrer constant, λ represents the wavelength of the electron beam which is equal to 1.5406 Å, β indicates the fwhm of the peak and θ is the Bragg's angle. The calculated crystallite size is listed in Table 1.

3.1.3. Microstructure of Nanoparticles by FE-SEM. FE-SEM was used to assess the surface and particle morphology. Figure 2c depicts the microstructure of a Ti-doped ZnO nanocomposite at two different magnifications. It is evident that the morphologies of the samples differ significantly from one another. This implies that the raw material has a profound impact on the morphologies of powders. As illustrated in Figure 2c, zinc acetate-derived powders exist in the form of rods with varying lengths. Sun et al. studied the change in morphology when different precursors were used. According to the report, the diffraction peak intensity of the (0 0 2) crystal face is stronger when the zinc salt is zinc acetate. PDF#36-1451.[34] The morphology of the produced nanocomposite is similar to that of a nanoflower, with ZnO having a spherical form and Ti having a needle-like structure. The Ti particles are

Figure 5. UV fluorescence of plant powder in different solvents (a) under open conditions, (b) visible light, (c) short 254 nm, and (d) long 365 nm.

Table 4. Color parameters of *T. terrestris* determined and the values obtained

| sample	L^*	a^*	b^*	ΔE
T. terrestris	64.90 ± 1.47^b	0.466 ± 1.32^a	20.10 ± 0.655^a	2.27 ± 1.21^a
TTE	30.566 ± 2.40^a	11.80 ± 1.44^b	15.40 ± 0.529^b	38.025 ± 1.9^b

Values are given as mean $\pm$ SD (n = 3). Different letters in the same column indicate significant differences ($p < 0.05$).

Table 5. Physical Parameters of Extract

test	percentage
moisture of the plant powder	0.48%
ash value of plant powder	0.19%
moisture content of extract	10.38%

Table 6. Crystallite Sizes of Cellulose

	X-ray diffraction analysis		
	crystallite sizes		
sample	L (nm) (101)	L (nm) (002)	crystallinity (%)
CNF	1.7024	2.81	67.32
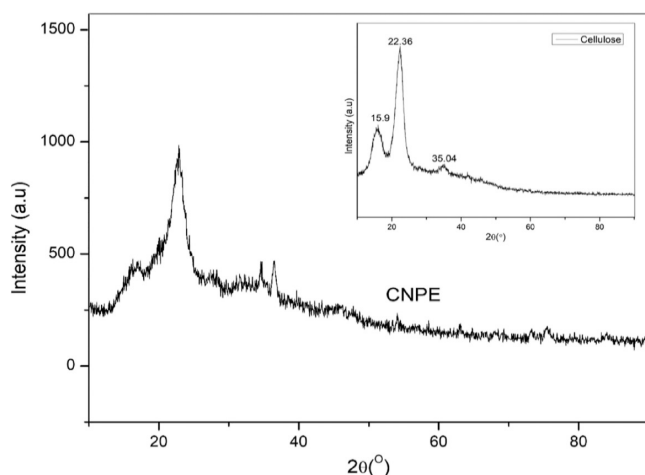
Figure 6. XRD spectrum of prepared nano cellulose and cellulose and CNPE scaffolds.
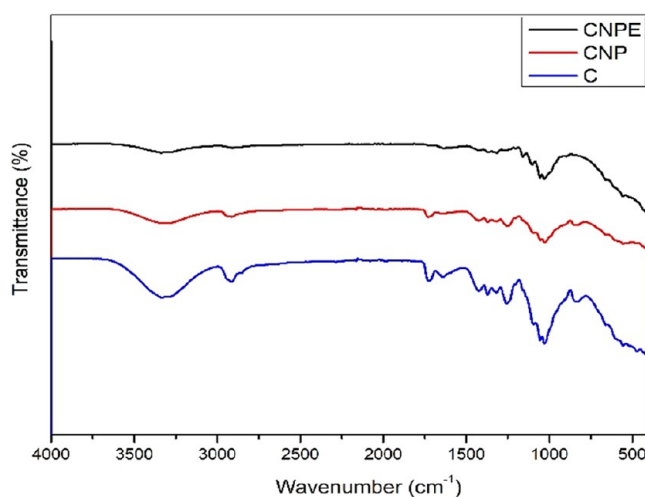
Figure 7. FTIR spectra of prepared films.

not aggregating and are equally dispersed on the spherical ZnO surface.[35] Table 2 indicates the elemental composition of the nanocomposite prepared (Figure 12).
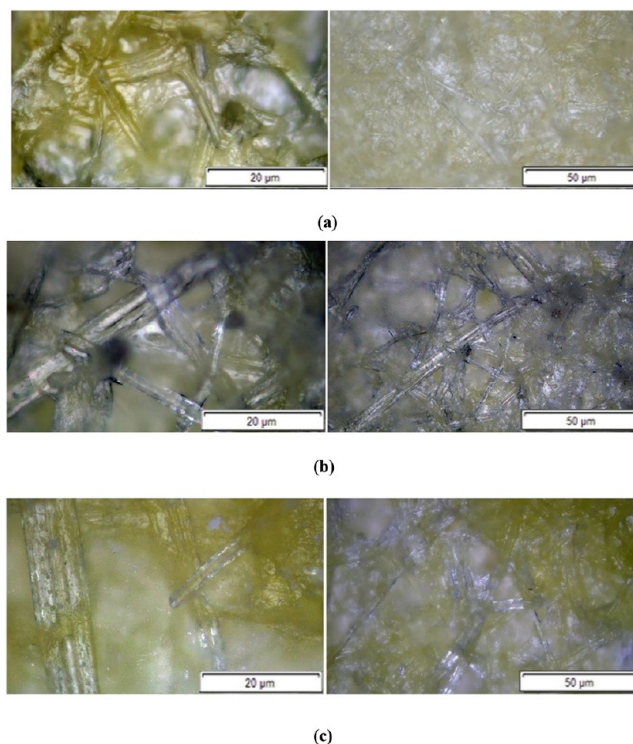
Figure 8. Optical microscope image of films prepared with (a) C, (b) CNP, and (c) CNPE.

3.2. Characterization of Extract. *3.2.1. Antimicrobial Property of Extract.* Three different cultures, two Gram-negative and one Gram-positive, were utilized to measure microbial activity and assess antibiotic susceptibility using either the disc diffusion method or the Kirby−Bauer method. Bayati et al. performed an antibacterial test by using Gentamycin as a reference.[36] The results clearly show that a higher extract content leads to a stronger resistance to microbes. *Staphylococcus aureus* and *E. coli* are Gram-positive and Gram-negative bacteria, respectively. From the study, the ethanol extract of TTE showed similar activity against all reference microorganisms. Significant efficacy was seen against *S. aureus*, *B. subtilis*, *B. cereus*, *C. diphtheriae*, *E. coli*, and *P. vulgaris* when using a 25% ethanol extract. The zone of inhibition exhibited by the extract against *S. aureus* and *E. coli* bacteria has a diameter of 16 and 18 mm, as mentioned in Table 3.

3.2.2. UV Spectra of TTE. The reasons for the UV shielding by TTE could be assigned to the alkaloids, glycosides, which can absorb UV rays. The plant contains saponins that do not produce UV absorption or have terminal absorption. Figure 4 shows the UV absorbance spectra with different concentrations. By lowering the concentration of the extract (2.5−0.16 mg/mL) the absorbance also reduces. These results demonstrated that the *T. terrestris* extract incorporated into the cellulose scaffold effectively obstructed UV light and imparted protective properties to human skin against UV radiation;
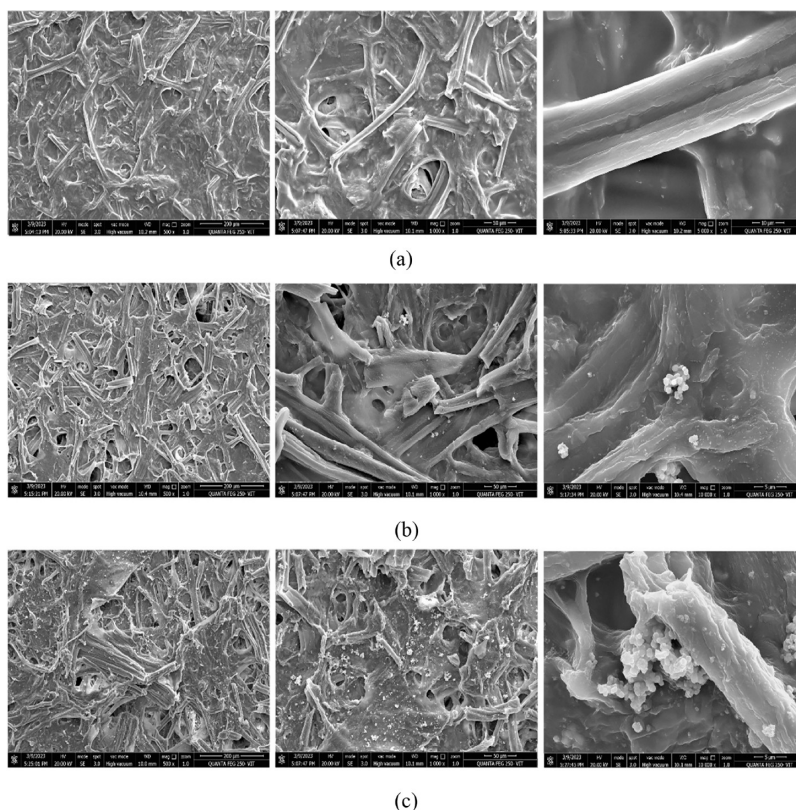
Figure 9. FE-SEM image of nanocellulose with different proportions: (a) C, (b) CNP, and (c) CNPE with different magnifications.

therefore, it has the potential to be utilized in medicinal applications.[37]

3.2.3. Physical Parameters of Extract. Figure 5 describes the fluorescence behavior of *T. terrestris* in visible light, the fluorescence with different solvents was determined under visible, short, and long UV light as mentioned in Table S1. The color parameters of *T. terrestris* were also determined and the values obtained were displayed in Table 4. We conducted a triplicate analysis and determined the standard deviation. The results of the moisture analysis and ash test are listed in Table 5. All the analysis was carried out on the basis of WHO guidelines for quality standardized herbal drugs.[26]

3.3. Structural Characterization and Yield of Cellulose. The yield of cellulose from sugar cane bagasse we obtained was 47.06%. From the previous reports, it is evident that the yield of sugar cane bagasse comes in the range of 40−50%. The crystallinity of nanocellulose, cellulose, and sugar cane bagasse has been evaluated by using X-ray diffractometry. Figure 4 shows that the fibers show increased orientation along a certain axis as the noncellulosic polysaccharides are removed and the amorphous zones disintegrate. The crystalline structure of extracted cellulose was investigated by X-ray diffractometry. The X-ray pattern of the cellulose exhibits the typical diffraction peaks of the crystalline structure of cellulose at 2θ = 15.9°, 22.36°, and 35.04°. Asem et al. reported that the XRD analysis reveals the presence of peaks at 2θ of 15.2° and 22°.[38] Percentage crystallinity of the samples was calculated from the XRD patterns using eq 9 and reported as 68 in, respectively, for cellulose. The crystallinity % and the L values are mentioned in Table 6.

$$\text{Crystallinity (\%)} = \frac{I_{002} - I_{am}}{I_{002}} \times 100 \qquad (9)$$

where I_{am} is the lowest intensity between the peaks of 2θ 15.9° and 22.3°, close to 18°, and I_{002} is the peak intensity at 2θ of 22.3. Because of the breakdown of glycosidic connections (depolymerization) in the cellulosic polymer chain, the rise in crystallinity in the nanocellulose sample was related to a decrease in matching amorphous domains. As a result, the amorphous regions were greatly reduced in the cellulose structure. The crystalline domains of cellulose chains were exceptionally resistant to hydrolysis and remained following pretreatment and depolymerization. Scherrer's formula was used to compute the crystallite sizes of the samples as per eq 10.

$$L = \frac{k\lambda}{\beta \cos\theta} \qquad (10)$$

where k = Scherrer constant (0.94), λ = X-ray wavelength (0.154059 nm), β = full-width half-maximum of the lattice plane reflection in radian, and θ = specific Bragg reflection angle. Table 6 depicts the crystallite sizes of several crystalline domains. The structural degradation of larger cellulose particles to tiny crystals of nanosize during acid hydrolysis was revealed by a notable decrease in intensity along with crystallite size at I_{002} (2θ = 22.3).

3.4. Structural Characterization of Films. The XRD pattern of the thin film samples was investigated and is depicted in Figure 4. All of the celluloses showed characteristic peaks of cellulose, with main 2 h diffraction angles close to 15.9 and 22.36 associated with the 101 and 002 crystalline planes, respectively. As a peak at 2θ corresponding to 19.23° and 40.67°, the figure clearly reveals the amorphous nature of cellulose film cross-linked with PVA. Because of the PVA inclusion, the cellulose in the spectrum has a low intensity. In
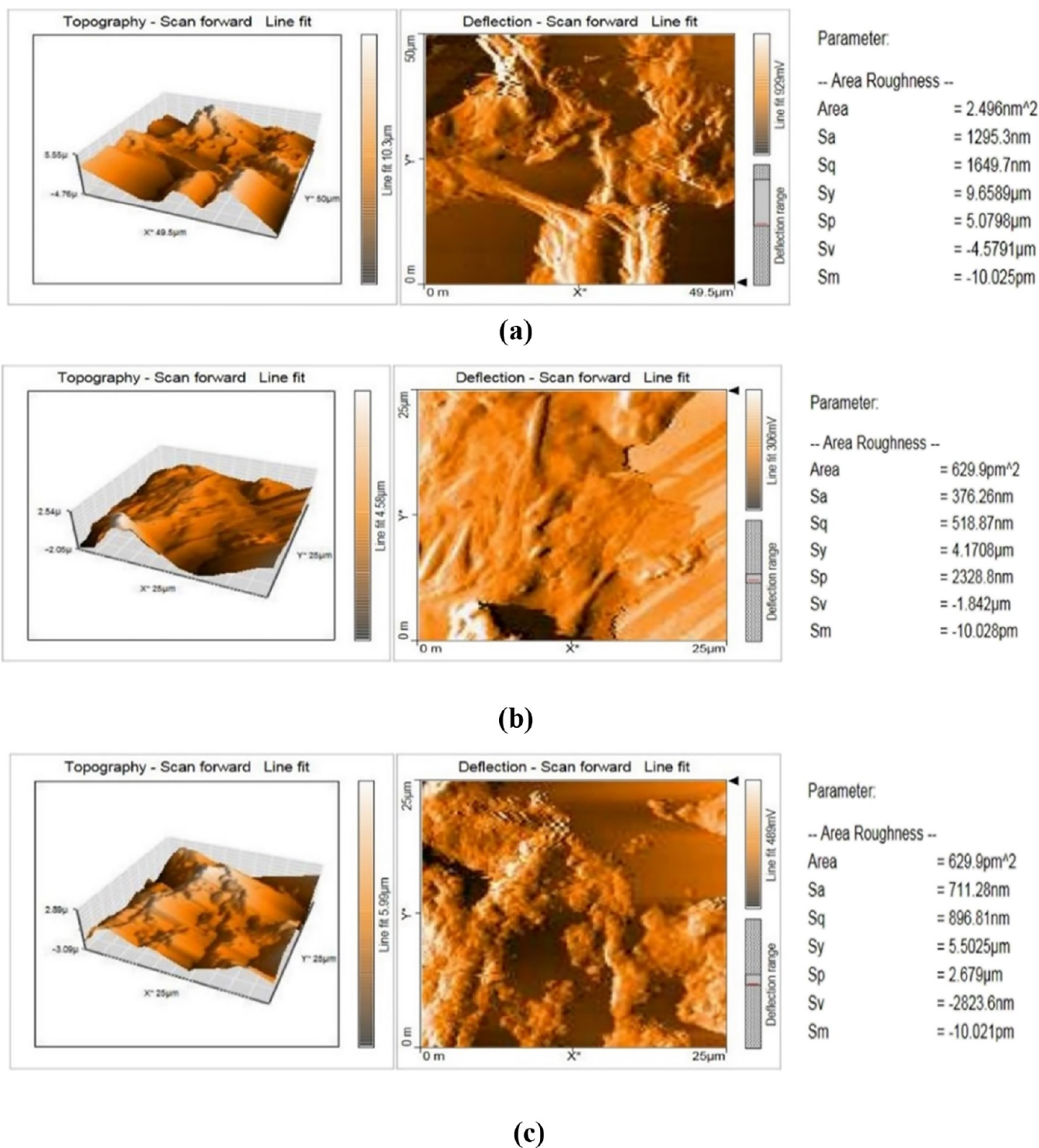
Figure 10. AFM image of thin film samples. (a) C, (b) CNP, and (c) CNPE.

comparison to C and CNPE, the film CNP is more crystalline. The surface of the cellulose sheet has clearly been covered with nanoparticles. Furthermore, the position of the CNP peak has altered, showing that the cellulose surface has been doped with hybrid nanoparticles. The existence of numerous oxygen-containing functional groups was shown by FTIR spectroscopy, as illustrated in Figure 6.

3.5. Fourier Transform Infrared Spectroscopy. The chemical characterization was performed through FTIR spectroscopy. FTIR spectra of purified cellulose (C) and the other two combinations of the same matrix are shown in Figure 7. From the spectrum, it was noted that one broad peak obtained in the range 3000−3500 cm^{-1} indicates the presence of OH and CH stretching. In addition, the spectra of each sample exhibited a distinctive C−H stretching vibration at 2894 cm^{-1}. The acetyl and uronic ester groups from pectin, hemicellulose, or the ester linkage of the carboxylic group of ferulic and p-coumaric acids of lignin and/or hemicellulose are primarily responsible for the C−O stretching vibration of the peak centered at 1730 cm^{-1} in the FTIR spectrum of ground
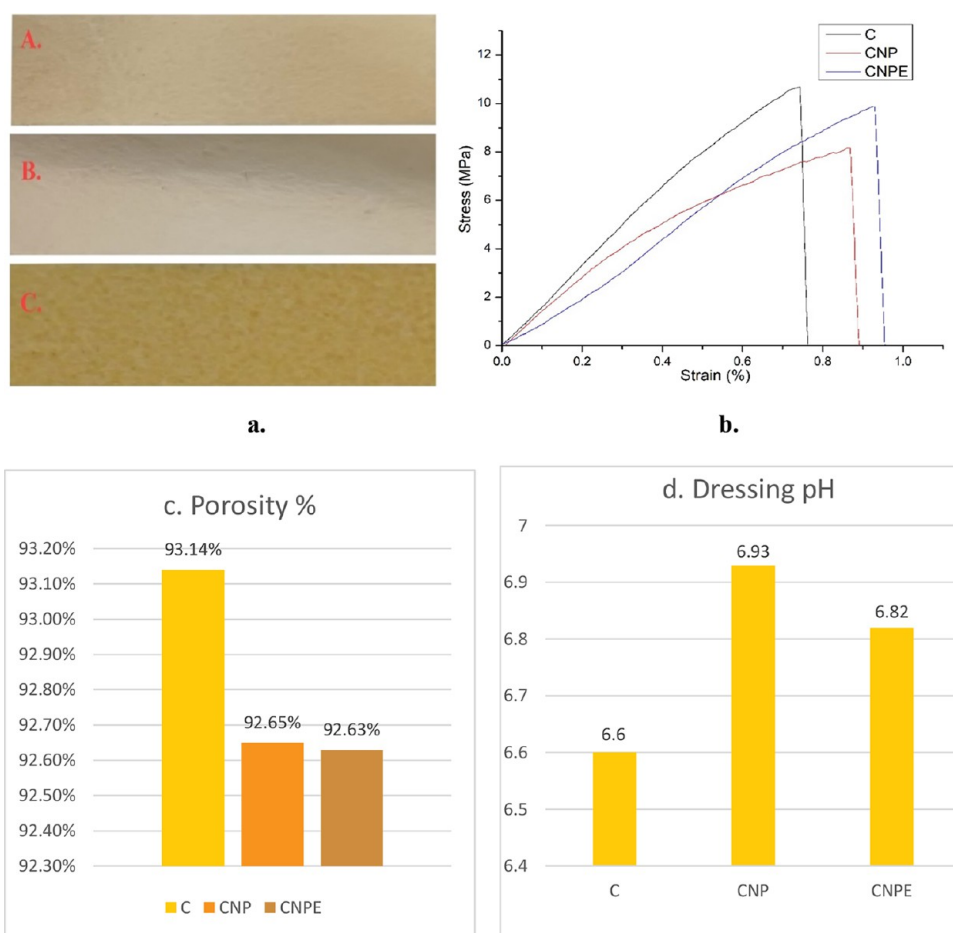
Figure 11. (a) Visual appearance of prepared films. (b) Stress vs strain graph of films. (c) Porosity %. (d) Dressing pH of (A) C, (B) CNP, (C) CNPE.

Table 7. Colour Values of Prepared Film[a]

sample	$L*$	$a*$	$b*$	ΔE	WI	YI
C	72.6 ± 0.26^b	0.433 ± 0.25^a	17.06 ± 0.64^b	0.725 ± 0.34^a	72.78 ± 0.32^a	33.570 ± 1.43^b
CNP	74.6 ± 2.35^b	1.733 ± 1.15^a	13.16 ± 1.99^a	5.178 ± 0.60^b	77.60 ± 0.15^c	25.201 ± 0.91^a
CNPE	62.46 ± 1.6^a	2.200 ± 1.10^a	41.13 ± 1.82^c	26.45 ± 1.75^c	67.3 ± 1.21^a	94.073 ± 0.52^a

[a]Values are given as mean $\pm$ SD ($n = 3$). Different letters in the same column indicate significant differences ($p < 0.05$).

Table 8. Physical Parameters of Film[a]

film formulations	thickness(mm)	elongation of break(%)	tensile strength (MPa)
C	0.076 ± 0.005^a	0.78	10.5
CNP	0.116 ± 0.025^b	0.89	8.2
CNPE	0.056 ± 0.005^a	0.96	9.1

[a]Values are given as mean $\pm$ SD ($n = 3$). Different letters in the same column indicate significant differences ($p < 0.05$).

sugar cane bagasse. Additionally, the bending vibration of the C−H and C−O bonds in the polysaccharide aromatic rings was linked to the vibration peak at 1365 cm^{-1} in all samples. The C−O out-of-plane stretching vibration of the aryl group in lignin is shown by the peak at 1245 cm^{-1}, which is mainly found in the spectra of bagasse. Additionally, the O−H bending of the adsorbed water is responsible for the absorbance peaks seen in the spectra of cellulose fibers generated after alkali treatment and nanocellulose in the range 1649−1641 cm^{-1}. The peak at 1056 cm^{-1} clearly shows C−

Table 9. Insulin

	absorbance at 630 nm				from graph $y = 0.001x$	
	triplicate 1	triplicate 2	triplicate 3	average	glucose final concentration μg/mL (initial 1000 μg/mL)	percentage glucose uptake
control (untreated)	0.691	0.682	0.686	0.686	686	31.4
25 μg/mL	0.425	0.418	0.407	0.417	417	58.3
50 μg/mL	0.296	0.306	0.314	0.305	305	69.5
100 μg/mL	0.116	0.105	0.113	0.111	111	88.9

Table 10. C-NP-E

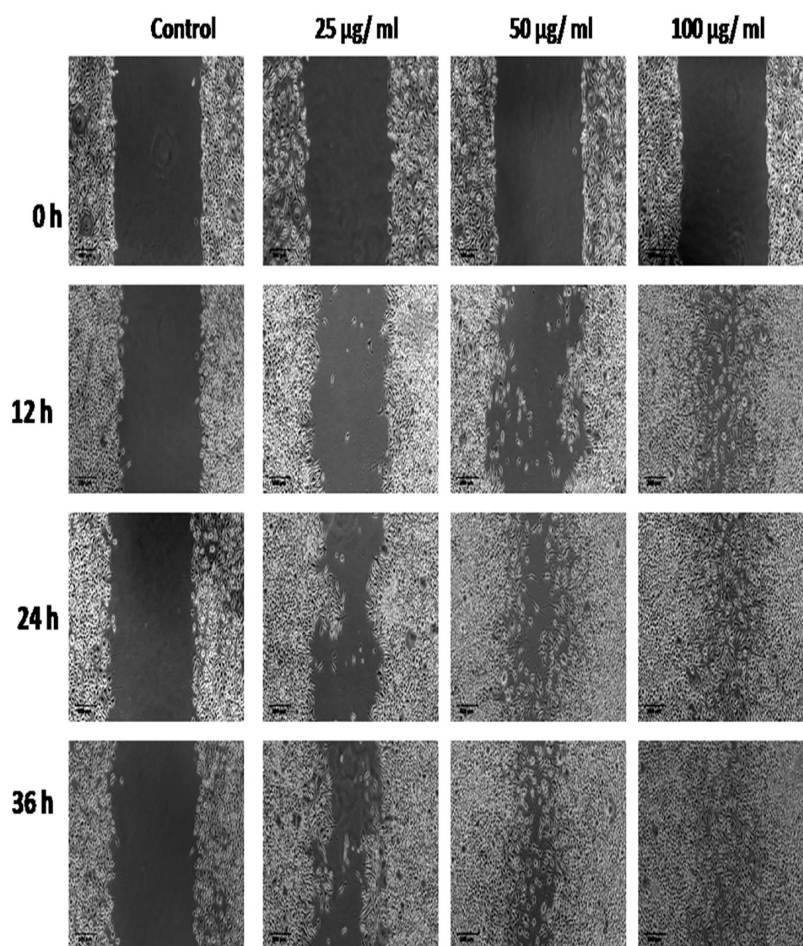|	absorbance at 630 nm				from graph $y = 0.001x$	
	triplicate 1	triplicate 2	triplicate 3	average	glucose final concentration μg/mL (initial 1000 μg/mL)	percentage glucose uptake
control (untreated)	0.697	0.677	0.691	0.688	688	31.20
25 μg/mL	0.601	0.592	0.587	0.593	593	40.70
50 μg/mL	0.504	0.495	0.509	0.503	503	49.70
100 μg/mL	0.421	0.413	0.401	0.412	412	58.80

Figure 12. In vitro scratch wound healing activity of CNPE film at different concentrations with different time interval.

O−C stretching vibrations in all samples. There is a slight change in the peak when we add TTE extract to the film.

3.6. Optical Microscopy and Field-Emission Scanning Electron Microscopy. Figures 8 and 9 show optical and FE-SEM images of thin films. The cellulose fiber structure is clearly seen in all the images. The removal of noncellulosic components such as hemicellulose and lignin by chemical treatment has enhanced defibrillation. The fiber bundles were separated into individual microsized fibers, resulting in a reduction in diameter.[39] The outcomes of the optical microscope investigation and the FE-SEM results are consistent. It is evident from the optical images that fibers have crystalline structures due to the removal of hemicellulose and lignin. The distinct layers formed by the combined acid/alkali pretreatment show a fiber with a larger surface area, while the cracks indicate greater porosity, leading to physical disorganization of the fibers. The image of the CNP film shows the even distribution of nanoparticles on the surface of cellulose fiber. The base matrix changes with the addition of

the extract, resulting in an improved film texture compared to the other film samples.

3.7. Atomic Force Microscopic Image of Thin Film. The surface topography of fibrous materials was studied using atomic force microscopy (AFM) technology. All polymer fiber materials have smooth surfaces with flattened surface shapes. The smoothness of the nanofiber was exhibited by using a color contrast of dark and light brown. An increase in color contrast indicates an increase in the size of the fiber. The maximum peak height (Sp), the maximum pit depth (Sv), the average surface roughness (Sa), and the surface roughness (Sq) were all calculated using the AFM topography, as shown in Figures 10. In the control film or 376.26 nm, the surface roughness value is quite low. The roughness value increased to 1295.3 nm with the inclusion of nanoparticles. The roughness value was again decreased to 711.28 nm by introducing the TTE.

3.8. Color Parameters of Film. The appearance of the films is shown in Figure 11a. The prepared films were extracted
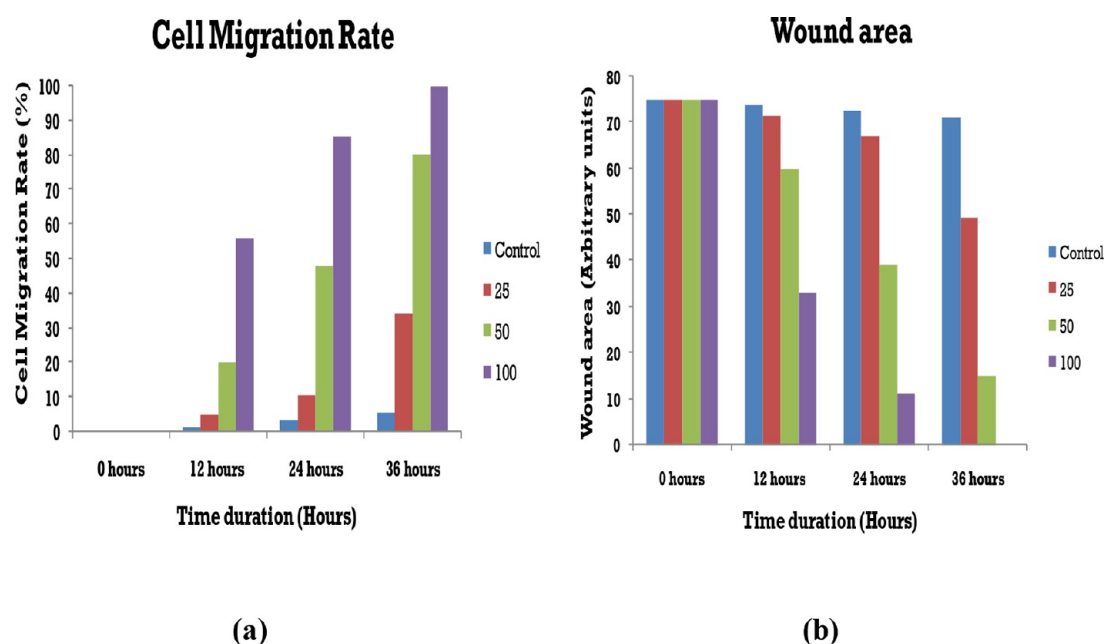
Figure 13. Bar graph representing (a) cell migration rate and (b) wound area and the healing efficacy with CNPE film.

from cellulose as the base matrix. From Table 7, it is evident that the WI value of the CNP film is high (77.60 ± 0.15) compared with other polymers.The reason behind the high WI is the incorporation of Ti/ZnO nanocomposites. For the CNPE film, the value is very low because of the TTE influence (Table 7). The YI value of the CNPE film is very large 94.073 $\pm$ 0.52. The *b* value (41.13 ± 1.82) of the film also increases in the case of CNPE films. The incorporation of extract in the film yellowness value increases more with an increase in concentration (Table 8).

3.9. Mechanical Properties of the Film. The mechanical strength of each polymer was tested by following the ASTM standard (ASTM D882-18). From Figure 11b, it is evident that CNPE has low tensile strength compared with different compositions of polymers. The nanoparticle incorporation results in no further change in the control film. It is noted that from previous results, changing the concentration of extract can alter the tensile properties of the film.

3.10. Porosity. The porosity of wound dressings is an important element to consider since it impacts the absorption capacity of exudates from the wound, which can lower the chances of infection.[40] The hemostatic dressings used must be able to absorb blood in order to activate the exogenous coagulation process and aid in endogenous coagulation. The collagen materials utilized for hemostasis and wound dressings are predominantly sponge products. As a result, the porosity and water absorption ratios serve as vital indices.

As demonstrated in Figure 11c, all of the bioscaffolds had porosities ranging from 92 to 94%. The porosity of the optimal hemostatic material should be at least 90%, although pure collagen sponge porosity can sometimes reach 90%. The produced material's porosity was determined and presented as a bar graph. For all three films, the obtained porosity was greater than 90%. Meanwhile, the aerogels' surface wettability was good. The initially measured contact angle was quite small, making the measurement almost impossible to do. The scaffold has a high propensity to absorb water, making it super-hydrophilic.

3.11. Wound Dressing pH. In a wound dressing, the pH of the dressing is a very important aspect. For promoting the proliferation of fibroblasts and preventing infections at the wound surface, an environment that is slightly acidic offers the optimal balance for the healing process of burns. A dressing pH of 6.82 was observed in the nanocomposites that were loaded with extract, as shown in Figure 11d. Previously reported literature values for 13 different commercial wound care products are consistent with these values.

3.12. Glucose Uptake Study. The rationale for using L6 cells for studying glucose transport has been well established.[41] The effect of CNPE's glucose uptake was determined to analyze their antidiabetic efficacies. Hyperglycemia occurs when the blood has an abnormally high level of sugar (glucose). High blood sugar is also known as high blood glucose. This occurs when the body has insufficient insulin (a hormone) or when the body is unable to properly use insulin (insulin resistance). Insulin stimulates glucose uptake in L6 cells; however, insulin that possesses a brief half-life encounters challenges in sustaining prolonged high activity. Insulin was found to be enhancing the glucose uptake in L6 cells in a concentration-dependent manner compared to untreated cells (control). The highest glucose uptake activity was shown by insulin at a concentration of 100 μg/mL. Tables 9 and 10 show the glucose uptake percentage of insulin (control) and the test sample. The studied sample was found to be enhancing the glucose uptake in L6 cells compared to untreated cells (control). The glucose uptake was found to be increasing in a concentration-dependent manner also. The highest glucose uptake activity was shown by the sample at a concentration of 100 μg/mL. The results indicate that the test compound may have type 2 antidiabetic properties and can be considered as a promising wound dressing candidate against insulin-resistant hyperglycemia.

3.13. In Vitro Wound Healing Studies. The representative photomicrographs showed that the sample had a significant impact on wound healing. It was found that the effectiveness of wound healing was time- and concentration-dependent. The concentration of 100 g/mL over the course of

36 h produced the greatest efficacy. This shows that the sample can be applied to human cells even when there are cuts or wounds or can be developed therapeutically as a wound-healing agent. A concentration- and time-dependent pattern of the increased cell migration rate, an indication of improved wound healing, is shown in Figure 13. The sample at 100 g/mL showed the highest level of effectiveness. Furthermore, concentration- and time-dependent decreases in the wound area were seen. The sample's 100 g/mL concentration showed the highest level of effectiveness.

4. CONCLUSIONS

In this study, nanocellulose/Ti-ZnO/TTE-based hydrogels were prepared by casting technique for usage in wound dressing applications. The extraction of nanocellulose was done through a steam explosion method. The prepared material is nontoxic and harmless for the environment, and one major benefit of the scaffold is water absorption capability. Due to its super hydrophilicity behavior, the material is good for the removal of fluids from the wound surface. By adding the natural extract, the active compounds present in the TTE will enhance the overall property. It is evident that the prepared scaffold shows good results with wound healing. The glucose uptake assay and scratch wound healing assay results show that the material shows wound healing capability. The CNPE scaffolds prepared have great clinical potential to be applied as a wound dressing.

■ ASSOCIATED CONTENT

Data Availability Statement

No data was used for the research described in the article.

ⓢ Supporting Information

The Supporting Information is available free of charge at https://pubs.acs.org/doi/10.1021/acsomega.4c00174.

> Cellulose extraction procedure and appearance of sample in different solvents and its color appearance (PDF)

■ AUTHOR INFORMATION

Corresponding Author

> **Dhanaraj Sangeetha** − *Department of Chemistry, SAS, Vellore Institute of Technology, Vellore 632 014, India;* ⓞ orcid.org/0000-0001-5834-9780; Email: dsangeetha@vit.ac.in

Authors

> **Jijo Thomas Koshy** − *Department of Chemistry, SAS, Vellore Institute of Technology, Vellore 632 014, India*
> **Yogesh Bele** − *Department of Microbiology, Sant Gadge Baba Amravati University, Amravati 444602, India*
> **Murugan Rakshitha** − *Department of Chemistry, SAS, Vellore Institute of Technology, Vellore 632 014, India*

Complete contact information is available at:
https://pubs.acs.org/10.1021/acsomega.4c00174

Author Contributions

D.S. and J.T.K. contributed equally. All authors have approved the final version of the manuscript.

Notes

The authors declare no competing financial interest.

■ ACKNOWLEDGMENTS

■ ABBREVIATIONS

T. terrestris: *Tribulus terrestris* powder
TTE: *Tribulus terrestris* extract
C: cellulose film
CNP: cellulose/ZnO-Ti film
CNPE: cellulose/ZnO-Ti/TTE film
XRD: X-ray diffraction
FTIR: Fourier-transform infrared spectroscopy
AFM: atomic force microscopy
FE-SEM: field emission-scanning electron microscopy
CTAB: cetyltrimethylammonium bronide
fwhm: full width at half-maximum
Sp: maximum peak height
Sv: maximum pit depth
Sa: average surface roughness
Sq: surface roughness
DMEM: Dulbecco's modified Eagle medium
PVA: poly(vinyl alcohol)
DMSO: dimethyl sulfoxide

■ REFERENCES

(1) Biswas, A.; Maiti, P.; Sahu, M. Polymeric Vehicles for Controlled Delivery of Ayurvedic Drugs for Wound Management. In *Biomedical Translational Research*; Springer Nature Singapore: Singapore, 2022; pp 585−599.

(2) Yildirimer, L.; Thanh, N. T. K.; Seifalian, A. M. Skin Regeneration Scaffolds: A Multimodal Bottom-up Approach. *Trends Biotechnol* **2012**, *30* (12), 638−648.

(3) Chouhan, D.; Chakraborty, B.; Nandi, S. K.; Mandal, B. B. Role of Non-Mulberry Silk Fibroin in Deposition and Regulation of Extracellular Matrix towards Accelerated Wound Healing. *Acta Biomater* **2017**, *48*, 157−174.

(4) Dhivya, S.; Padma, V. V.; Santhini, E. Wound Dressings − a Review. *Biomedicine (Taipei)* **2015**, *5* (4), 22.

(5) Koshy, J.; Sangeetha, D. Recent Progress and Treatment Strategy of Pectin Polysaccharide Based Tissue Engineering Scaffolds in Cancer Therapy, Wound Healing and Cartilage Regeneration. *Int. J. Biol. Macromol.* **2024**, *257*, No. 128594.

(6) Michel, T.; Destandau, E.; Le Floch, G.; Lucchesi, M. E.; Elfakir, C. Antimicrobial, Antioxidant and Phytochemical Investigations of Sea Buckthorn (Hippophaë Rhamnoides L.) Leaf, Stem, Root and Seed. *Food Chem.* **2012**, *131* (3), 754−760.

(7) Kim, J.; Lee, C.-M. Wound Healing Potential of a Polyvinyl Alcohol-Blended Pectin Hydrogel Containing Hippophae Rahmnoides L. Extract in a Rat Model. *Int. J. Biol. Macromol.* **2017**, *99*, 586−593.

(8) Gopinath, V.; Kamath, S. M.; Priyadarshini, S.; Chik, Z.; Alarfaj, A. A.; Hirad, A. H. Multifunctional Applications of Natural Polysaccharide Starch and Cellulose: An Update on Recent Advances. *Biomedicine & Pharmacotherapy* **2022**, *146*, No. 112492.

(9) Yang, Y.; Lu, Y.; Zeng, K.; Heinze, T.; Groth, T.; Zhang, K. Recent Progress on Cellulose-Based Ionic Compounds for Biomaterials. *Adv. Mater.* **2021**, *33* (28), No. 2000717.

(10) Mali, P.; Sherje, A. P. Cellulose Nanocrystals: Fundamentals and Biomedical Applications. *Carbohydr. Polym.* **2022**, *275*, No. 118668.

(11) George, J.; Sabapathi, S. N. Cellulose Nanocrystals: Synthesis, Functional Properties, and Applications. *Nanotechnol. Sci. Appl.* **2015**, *8*, 45−54.

(12) Meng, X.; Ragauskas, A. J. Recent Advances in Understanding the Role of Cellulose Accessibility in Enzymatic Hydrolysis of Lignocellulosic Substrates. *Curr. Opin Biotechnol* **2014**, *27*, 150−158.

(13) Mu, R.; Hong, X.; Ni, Y.; Li, Y.; Pang, J.; Wang, Q.; Xiao, J.; Zheng, Y. Recent Trends and Applications of Cellulose Nanocrystals in Food Industry. *Trends Food Sci. Technol.* **2019**, *93*, 136−144.

(14) Zhang, Q.; Zhang, L.; Wu, W.; Xiao, H. Methods and Applications of Nanocellulose Loaded with Inorganic Nanomaterials: A Review. *Carbohydr. Polym.* **2020**, *229*, No. 115454.

(15) Raghav, N.; Sharma, M. R.; Kennedy, J. F. Nanocellulose: A Mini-Review on Types and Use in Drug Delivery Systems. *Carbohydrate Polymer Technologies and Applications* **2021**, *2*, No. 100031.

(16) Miyazawa, T.; Itaya, M.; Burdeos, G. C.; Nakagawa, K.; Miyazawa, T. A Critical Review of the Use of Surfactant-Coated Nanoparticles in Nanomedicine and Food Nanotechnology. *Int. J. Nanomedicine* **2021**, *16*, 3937−3999.

(17) Kumar, D.; Rub, M. A. Interaction of Metal Ion-Coordinated Dipeptide Complex and Ninhydrin in the Alkanediyl-α,Ω-bis-Type Gemini Surfactant System. *J. Surfactants Deterg* **2019**, *22* (6), 1299−1308.

(18) Khalid, A.; Nadeem, T.; Khan, M. A.; Ali, Q.; Zubair, M. In Vitro Evaluation of Immunomodulatory, Anti-Diabetic, and Anti-Cancer Molecular Mechanisms of Tribulus Terrestris Extracts. *Sci. Rep* **2022**, *12* (1), 22478.

(19) Sun, X.-C.; Song, X.; Guo, F.; Yuan, Y.-H.; Wang, S.-Y.; Wang, S.; Liu, K.-L.; Lv, X.-Y.; Han, B.; Zhang, C.; Liu, J.-T. Terrestrosin D, a Spirostanol Saponin from Tribulus Terrestris L. with Potential Hepatorenal Toxicity. *J. Ethnopharmacol* **2022**, *283*, No. 114716.

(20) Misiakiewicz-Has, K.; Maciejewska-Markiewicz, D.; Rzeszotek, S.; Pilutin, A.; Kolasa, A.; Szumilas, P.; Stachowska, E.; Wiszniewska, B. The Obscure Effect of Tribulus Terrestris Saponins Plus Inulin on Liver Morphology, Liver Fatty Acids, Plasma Glucose, and Lipid Profile in SD Rats with and without Induced Type 2 Diabetes Mellitus. *Int. J. Mol. Sci.* **2021**, *22* (16), 8680.

(21) Figueiredo, C. C. M.; da Costa Gomes, A.; Granero, F. O.; Bronzel Junior, J. L.; Silva, L. P.; Ximenes, V. F.; da Silva, R. M. G. Antiglycation and Antioxidant Activities of the Crude Extract and Saponin Fraction of Tribulus Terrestris before and after Microcapsule Release. *J. Integr Med.* **2022**, *20* (2), 153−162.

(22) Casanova, F.; Freixo, R.; Pereira, C. F.; Ribeiro, A. B.; Costa, E. M.; Pintado, M. E.; Ramos, O. L. Comparative Study of Green and Traditional Routes for Cellulose Extraction from a Sugarcane By-Product. *Polymers (Basel)* **2023**, *15* (5), 1251.

(23) Sriwong, C.; Boonrungsiman, S.; Sukyai, P. Sugarcane Bagasse Cellulose-Based Scaffolds Incorporated Hydroxyapatite for Promoting Proliferation, Adhesion and Differentiation of Osteoblasts. *Ind. Crops Prod* **2023**, *192*, No. 115979.

(24) Ali, M. M.; Haque, Md. J.; Kabir, M. H.; Kaiyum, M. A.; Rahman, M. S. Nano Synthesis of ZnO−TiO2 Composites by Sol-Gel Method and Evaluation of Their Antibacterial, Optical and Photo-catalytic Activities. *Results in Materials* **2021**, *11*, No. 100199.

(25) Valgas, C.; Souza, S. M. de; Smânia, E. F. A.; Smânia, A., Jr Screening Methods to Determine Antibacterial Activity of Natural Products. *Brazilian Journal of Microbiology* **2007**, *38* (2), 369−380.

(26) Khandelwal, K. R. *Practical Pharmacognosy*, 23rd edition; Nirali Prakashan, 2013.

(27) Koshy, J. T.; Vasudevan, D.; Sangeetha, D.; Prabu, A. A. Biopolymer Based Multifunctional Films Loaded with Anthocyanin Rich Floral Extract and ZnO Nano Particles for Smart Packaging and Wound Healing Applications. *Polymers (Basel)* **2023**, *15* (10), 2372.

(28) Venkatesan, J.; Bhatnagar, I.; Kim, S.-K. Chitosan-Alginate Biocomposite Containing Fucoidan for Bone Tissue Engineering. *Mar Drugs* **2014**, *12* (1), 300−316.

(29) Suthar, M.; Rathore, G.; Basniwal, P.; Jain, D.; Gupta, R.; Pareek, A. Study of Glucose Uptake Activity of *Helicteres Isora* Linn. Fruits in L-6 Cell Lines. *Int. J. Diabetes Dev Ctries* **2009**, *29* (4), 170.

(30) Anitha, S.; Brabu, B.; Thiruvadigal, D. J.; Gopalakrishnan, C.; Natarajan, T. S. Optical, Bactericidal and Water Repellent Properties of Electrospun Nano-Composite Membranes of Cellulose Acetate and ZnO. *Carbohydr. Polym.* **2012**, *87* (2), 1065−1072.

(31) Wetchakun, N.; Incessungvorn, B.; Wetchakun, K.; Phanichphant, S. Influence of Calcination Temperature on Anatase to Rutile Phase Transformation in TiO2 Nanoparticles Synthesized by the Modified Sol−Gel Method. *Mater. Lett.* **2012**, *82*, 195−198.

(32) Menazea, A. A.; Abdelghany, A. M.; Osman, W. H.; Hakeem, N. A.; El-Kader, F. H. A. Precipitation of Silver Nanoparticles in Silicate Glasses via Nd:YAG Nanosecond Laser and Its Character-ization. *J. Non Cryst. Solids* **2019**, *513*, 49−54.

(33) El-Kader, F. H. A.; Hakeem, N. A.; Osman, W. H.; Menazea, A. A.; Abdelghany, A. M. Nanosecond Laser Irradiation as New Route for Silver Nanoparticles Precipitation in Glassy Matrix. *Silicon* **2019**, *11* (1), 377−381.

(34) Sun, T.; Hao, H.; Hao, W.; Yi, S.; Li, X.; Li, J. Preparation and Antibacterial Properties of Titanium-Doped ZnO from Different Zinc Salts. *Nanoscale Res. Lett.* **2014**, *9* (1), 98.

(35) Pant, H. R.; Park, C. H.; Pant, B.; Tijing, L. D.; Kim, H. Y.; Kim, C. S. Synthesis, Characterization, and Photocatalytic Properties of ZnO Nano-Flower Containing TiO2 NPs. *Ceram. Int.* **2012**, *38* (4), 2943−2950.

(36) Al-Bayati, F. A.; Al-Mola, H. F. Antibacterial and Antifungal Activities of Different Parts of Tribulus Terrestris L. Growing in Iraq. *J. Zhejiang Univ Sci. B* **2008**, *9* (2), 154−159.

(37) Rehan, M.; Barhoum, A.; Van Assche, G.; Dufresne, A.; Gätjen, L.; Wilken, R. Towards Multifunctional Cellulosic Fabric: UV Photo-Reduction and in-Situ Synthesis of Silver Nanoparticles into Cellulose Fabrics. *Int. J. Biol. Macromol.* **2017**, *98*, 877−886.

(38) Asem, M.; Noraini Jimat, D.; Huda Syazwani Jafri, N.; Mohd Fazli Wan Nawawi, W.; Fadhillah Mohamed Azmin, N.; Firdaus Abd Wahab, M. Entangled Cellulose Nanofibers Produced from Sugarcane Bagasse via Alkaline Treatment, Mild Acid Hydrolysis Assisted with Ultrasonication. *Journal of King Saud University - Engineering Sciences* **2023**, *35* (1), 24−31.

(39) Deepa, B.; Abraham, E.; Cordeiro, N.; Mozetic, M.; Mathew, A. P.; Oksman, K.; Faria, M.; Thomas, S.; Pothan, L. A. Utilization of Various Lignocellulosic Biomass for the Production of Nanocellulose: A Comparative Study. *Cellulose* **2015**, *22* (2), 1075−1090.

(40) Poonguzhali, R.; Khaleel Basha, S.; Sugantha Kumari, V. Novel Asymmetric Chitosan/PVP/Nanocellulose Wound Dressing: In Vitro and in Vivo Evaluation. *Int. J. Biol. Macromol.* **2018**, *112*, 1300−1309.

(41) Koivisto, U. M.; Martinez-Valdez, H.; Bilan, P. J.; Burdett, E.; Ramlal, T.; Klip, A. Differential Regulation of the GLUT-1 and GLUT-4 Glucose Transport Systems by Glucose and Insulin in L6Muscle Cells in Culture. *J. Biol. Chem.* **1991**, *266* (4), 2615−2621.